

Effects of Test Temperature and Loading Conditions on the Tensile Properties of a Zr-Based Bulk Metallic Glass

A.H. VORMELKER, O.L. VATAMANU, L. KECSKES, and J.J. LEWANDOWSKI

The effects of changes in test temperature (20C, 260 C, 330 C, and 380 C), strain rate (10^{-5} to 10^{-1} s $^{-1}$), and loading conditions (displacement control vs loading-rate control) on the tensile behavior of Zr_{41.2}Ti_{13.8}Cu_{12.5}Ni₁₀Be_{22.5} (LiquidMetal 1 (LM1)), a bulk metallic glass (BMG), have been determined. Significant effects of the test temperature, strain rate, and loading condition were observed on the strength, ductility/elongation, and mechanisms of failure (shear, ductile rupture, etc.). This material exhibited extensive elongation (i.e., >100 pct) prior to failure when tested near the glass transition temperature ($T_g = 375$ C) at sufficiently low strain rates, while higher strain rates or lower test temperatures produced shear fracture at low elongation. The flow and fracture behavior was also significantly affected by the loading condition (i.e., displacement vs loading-rate control). The effective strain rate necessary to cause failure in shear without significant global flow was several orders of magnitude lower in loading-rate control than in displacement control. Samples exhibiting high elongation tested in displacement control gently and convexly drew to a near point (i.e., ductile rupture). Samples tested at the same temperature exhibiting high elongation in loading-rate control rapidly and concavely necked, followed by drawing to a constant diameter (wire draw), (ductile drawing), eventually failing by nearly pure ductile rupture. All samples that displayed significant elongation did so inhomogeneously, and were characterized by non-Newtonian global flow.

DOI: 10.1007/s11661-007-9410-4

The Minerals, Metals & Materials Society and ASM International 2007

I. INTRODUCTION

METALLIC glasses have been produced in bulk sizes (i.e., >1 mm) for more than a decade. The size of these bulk metallic glasses (BMGs), combined with their high strengths and high elastic limits, make them appealing candidates for structural applications.^[1] LiquidMetal 1 (LM1), formerly Vitreloy 1, of the composition Zr_{41.2}Ti_{13.8}Cu_{12.5}Ni₁₀Be_{22.5}, is one of the most commercially-available BMGs, due to relatively sluggish recrystallization kinetics and, thus, its low critical cooling rate.^[2] It is also the most heavily studied BMG. The thermodynamic, kinetic, toughness, and compressive viscoelastic properties have been well characterized.^[3...6] However, tension testing has primarily been limited to room-temperature conditions for

LM1.^[5,6] Relatively few high-temperature tensile studies have been conducted on BMGs (e.g., Reference 7).

The flow and fracture behavior of BMGs is quite different than that of ordinary crystalline metals. Spaepen classified the plastic flow of metallic glass to be either homogeneous or inhomogeneous, and adapted a free volume model^[8] originally developed for polymers^[9] to describe the flow. Inhomogeneous catastrophic shear failure at low macroscopic strains was expected at all strain rates applied at temperatures well below the T_g . In the Spaepen free volume model, flow occurs when a hydrostatic tensile stress causes a critical amount of hydrostatic dilatation (expansion). A rapid increase in free volume is proposed to occur in a thin layer of a plane, accompanied by a rapid loss of viscosity in that plane, resulting in local viscous flow at significantly reduced stresses.

At temperatures near the T_g , models predict homogeneous viscous flow at sufficiently low strain rates.^[8,10] Spaepen defined homogeneous flow as uniform deformation or, in other words, a constant cross-sectional area along the gage length during deformation to very high strains. Free volume is now assumed to remain constant, as all atoms present in the gage length rearrange themselves to the applied shear stress, resulting in viscous flow at sufficiently high temperatures and low strain rates. The rearrangement of atoms due to a mechanical stress or thermal annealing is also described as structural relaxation. Structural relaxation annihilates free volume, while mechanical stress causes generation of free volume, resulting in no net change. Structural relaxation increases with increasing

A.H. VORMELKER, formerly Graduate Student, Department of Materials Science and Engineering, Case Western Reserve University, is Plant Metallurgist, Marine Mechanical Corporation, 24703 Euclid Avenue, Cleveland, OH 44117, USA. O.L. VATAMANU, formerly, Post Doctorate Researcher with Case Western Reserve University, is Senior Research Scientist, Powdermet, Inc., Euclid, OH 44117, USA. L. KECSKES, Research Physical Scientist, is with the U.S. Army Research Laboratory, Aberdeen Proving Ground, MD 21005-5069, USA. J.J. LEWANDOWSKI, Leonard Case Jr. Professor of Engineering, Department of Materials Science and Engineering, Case Western Reserve University, Cleveland, OH 44106, USA. Contact e-mail: jjl3@case.edu

This article is based on a presentation given in the symposium entitled "Bulk Metallic Glasses IV," which occurred February 25... March 1, 2007 during the TMS Annual Meeting in Orlando, Florida under the auspices of the TMS/ASM Mechanical Behavior of Materials Committee.

Article published online December 21, 2007

temperature and decreasing strain rate (e.g., annealing to reduce free volume). Mechanical generation of free volume increases with an increase in strain rate.

In many compression and nearly all tension studies to date, BMGs have been found to fracture inhomogeneously in catastrophic shear at room temperature. Reduction in the compression sample aspect ratio^[4] has produced increased compressive ductility in both quasi-static^[11,12] and dynamic testing.^[13] The intrinsic plasticity of amorphous metals was suggested in early work^[14,15] to be controlled by the Poisson ratio. More recent work^[16...18] has explored the effects of systematic changes in Poisson ratio (e.g., via changes in chemistry or annealing treatment) on ductility^[16...20] and toughness,^[16] with significant increases in plasticity accompanying higher Poisson ratios, as reviewed elsewhere.^[21]

Compression tests of many BMGs, conducted at sufficiently low strain rates near the T_g , have reported •homogeneous• flow, also in agreement with Spaepen free volume theory. However, the cross-sectional area was not monitored in these studies,^[4,22...26] and deformation was assumed to be uniform and thus homogeneous. While this permits calculation of true stress, the assumption of the conservation of volume has not been explicitly confirmed for BMGs deforming in the homogeneous flow regime.^[4]

Recent compression studies conducted near the T_g of parallelepiped and cylindrical specimens have further defined homogeneous flow as either Newtonian or non-Newtonian.^[4,22...26] Newtonian flow is defined to occur when the measured stress is linearly proportional to the applied strain rate (i.e., $\tau / \dot{\gamma}$).^[27] In addition, the power law must be obeyed, where the strain-rate-sensitivity value (m) must equal 1, as in the equation $\sigma = K \dot{\epsilon}^m$, where $\dot{\epsilon}$ is the true strain rate, σ is the flow stress, and K is a constant.^[7] These constraints result in a material viscosity that is independent of strain rate.

In conditions found to exhibit Newtonian flow, the maximum true stress obtained in compression is found to be approximately equal to the steady-state stress.^[4,22...26,28...31] Here, stress becomes constant with respect to strain, at some strain value after the maximum stress is reached. This steady-state stress is typically used in the calculations that determine whether flow is Newtonian or non-Newtonian, where the strain rate is changed and the •steady-state stress• is measured.

At sufficiently high strain rates, a drop in true stress with increasing strain has been reported as •stress overshoots.^[4,22...26,28,30,32...34] The magnitude of the stress overshoot is typically reported to equal the difference between the maximum stress and the lower steady-state stress. However, stress overshoots have been reported in samples that did not achieve a steady-state stress, and in studies where real-time true stress was not documented.^[32...34] The true stresses and stress overshoots reported in some previous studies^[4,23,25] can be interpreted to represent a weakening of the material (i.e., strain softening) and attributed to a net increase in free volume. According to recent work,^[29,35] the increase in the true strain rate that accompanies the onset of plastic deformation results in a reduction of

structural-relaxation-induced free volume annihilation. The stress-induced free volume generation then dominates, resulting in a net increase in free volume. This reduces the material's viscosity and causes a drop in strength, resulting in what is termed the stress overshoot. Samples that exhibited stress overshoots were found to exhibit non-Newtonian flow.^[4,23...26]

While compression tests are invaluable for efficiently characterizing flow at a broad range of temperatures and strain rates, they have some limitations. Geometric hardening does not allow a true fracture stress to be attained. Friction causes barreling, making it difficult to determine whether homogeneous (i.e., uniform) deformation is occurring. Stress concentrations and the effects of changes in the aspect ratio (i.e., L/D) also have been shown to affect the data.^[13] Typically, uniform deformation has been assumed, based on visual observations.^[4,23,25,31] Mathematical corrections for barreling can be made,^[36] although it is not known whether these corrections were made in the cited works.

Unlike compression tests, tension tests allow true tensile fracture stress to be calculated and avoid the problems of end effects, friction, buckling, and geometric hardening. The existence of inhomogeneous flow is easily detected if necking occurs. Due to the added complexity of the specimen shape and loading fixtures, relatively few tension tests have been performed on metallic glasses near their T_g , most of which were performed on ribbons (e.g., References 28 and 30). These studies on ribbons reported large homogeneous elongations (attaining a steady-state stress), with the flow being Newtonian or non-Newtonian, depending on the temperature and strain rate applied. However, thin ribbons are subject to plane-stress conditions; these discourage the formation of a neck of the type present in cylindrical samples.

The tensile behavior near the T_g of a bulk Zr-10Al-5Ti-17.9Cu-14.6Ni metallic glass in sheet form (1.27-mm thick) was studied by Wadsworth and Nieh.^[7,33,37] Stress overshoots were primarily attributed to the loss of load-bearing capacity due to necking and not due to material softening via the generation of free volume. Flow was found to transition from Newtonian to non-Newtonian with increasing strain rate, as observed in ribbon samples by Kawamura et al.^[35] The authors proposed that the observed stress-induced crystallization was responsible for the non-Newtonian behavior exhibited in their studies, in contrast to the proposed increase in free volume to which the cause of the stress overshoots in other works has been attributed.^[29,35]

High-temperature tension studies were also performed on rectangular dog bone specimens of LM1 by Lee et al.^[32] and Wang et al.^[34] Lee conducted tension tests at two strain rates, at temperatures in the range of the T_g and T_x . Engineering stress-strain curves showed what appeared to be stress overshoots, which only reached steady state at sufficiently high temperatures and strain rates. Samples that displayed macroscopic deformation appeared to neck significantly, making flow inhomogeneous. Wang et al.^[34] conducted tension tests at various strain rates and temperatures, ranging from the T_g to well below the T_x . While fracture

morphologies were described by Wang et al.,^[34] no attempt was made in either study^[32,34] to characterize flow as Newtonian/non-Newtonian. It must also be noted that the rectangular dog bone sample geometry introduces stress concentrations at the corners, and raises the possibility of plane-strain conditions if thickness is not sufficient, thus restricting local necking.^[38]

Superplastic behavior has been reported to occur in metallic glasses in studies by Nieff,^[7,33,37] Lee,^[32] Wang,^[34] and many others, in both compression and tension (e.g., References 4 and 28). The definition of superplastic deformation varies, but is typically associated with elongations (i.e., engineering strains) greater than 100 to 1000 pct. In true superplastic behavior, a sample undergoes extensive deformation without pronounced necking.^[39] Macroscopic stress concentrators like surface scratches and incipient necks may exist, but should not deepen. Failure should occur in ductile rupture when the sample draws to a point.

In this study, the effects of changes in strain rate, test temperature, and loading condition (loading-rate vs displacement-rate control) on flow and fracture have been evaluated. Macroscopic (i.e., ductile, global) flow will be characterized as homogeneous or inhomogeneous based on the existence of a neck or a necklike feature. Macroscopic flow will be further characterized as Newtonian or non-Newtonian, and the existence of superplasticity will also be considered.

II. EXPERIMENTAL

A. Materials

Materials were received in the form of the dimensions 145 · 105 · 7.5 mm and a target composition of $Zr_{41.2}Ti_{13.8}Cu_{12.5}Ni_{10}Be_{22.5}$. Analysis by X-ray diffraction (XRD) was performed to determine the as-received structure. Rectangular specimens (20 · 12 · 7 mm) were metallographically polished to a 1 μ m finish and scanned on a Scintag X1 (Scintag, Inc., Sunnyvale, CA), using $Cu K_{\alpha}$ radiation over a range of 2θ of 20 to 120 deg. The T_g and T_x were determined at 20 K/min^[40] and converted to that expected at 10 K/min, by using the heating rate dependence of T_g and T_x found by Busch et al.^[41] The values of T_g and T_x estimated for 10 K/min are 375 C and 448 C, respectively.

B. Mechanical Tests

1. Hot microhardness testing

Hot microhardness tests were performed to estimate the strength of LM1 as a function of temperature,^[42] providing guidance for subsequent tension testing. A Nikon QM High-Temperature Microhardness Tester (Kawasaki, Japan) was used. Plates 5 · 5 · 10 mm in size were prepared with the indentation surface (i.e., 5 · 10 mm) metallographically polished. Samples were tested at a load of 300 g and a 15-second indentation time. After initial indentations at room temperature, the temperature was increased incrementally at 10 C/min and allowed to equilibrate for 3 minutes prior to making three indentations at each temperature, up to and

including 380 C. The indentation sizes were then measured at room temperature on a Buehler Micromet (Buehler Ltd., Lake Bluff, IL). The calculated effective strain rate was $10^{-5} s^{-1}$, consistent with other reports.^[43]

2. Uniaxial tension

Smooth, buttonhead cylindrical tension samples of LM1 were ground with a gage length of either 5 or 6 mm and a diameter of either 2 or 3 mm. The samples were subsequently metallographically polished with SiC grit papers using 0.1 μ m diamond pastes prior to testing in tension. Tension tests were conducted on an MTS 810 servohydraulic test machine (MTS Systems Corp., Eden Prairie, MN) in accordance with ASTM E8.^[44] In tests conducted above room temperature, the specimens were first heated at 7.5 to 10 K/min in an Applied Test Systems series 3710 environmental chamber (Applied Test Systems, Inc., Butler, PA) under loading-rate control with a small constant load. The desired test temperature was allowed to equilibrate by waiting until the displacement rate produced by thermal expansion of the test fixture dropped below 20 pct of the desired testing target rate, resulting in hold times of 5 to 65 minutes. This oven is certified to be uniform within ± 3 C at the temperatures studied. In addition to the oven temperature probe (near the back of the chamber), a thermocouple was placed adjacent to the tension sample, to assure that temperature uniformity was met. Tests were not performed until the sample thermal couple reading equaled the reading of the oven temperature probe. All initial samples were tested to failure while monitoring load and displacement. Some subsequent tests were interrupted after reaching certain combinations of stress and strain.

Tension tests were conducted in either displacement control or loading-rate control, at the temperatures, loading rates, and initial strain rates specified in Table I. Load and uniaxial displacement data were recorded, but real-time cross-sectional area measurements were not possible with the current test configuration. Sample dimensions after fracture or at the end of the interrupted tests were obtained optically or via scanning electron microscopy (SEM), when necessary. Fractography was conducted on a PHILIPS* XL-30 Environmental and a

*PHILIPS is a trademark of Philips Electronic Instruments Corp., Mahwah, NJ.

Hitachi 54500 high-resolution SEM (Hitachi Systems & Services, Ltd., Tokyo, Japan) at 15 kV.

III. RESULTS

A. Composition and Structure

The XRD trace of LM1 revealed very broad intensity peaks, typical of amorphous materials, as crystallographic planes are needed to produce sharp reflection of X-rays at well-defined angles of diffraction. Thus, no

Table I. Tension Testing Conditions

Temperature, C	Control	Rate	$\dot{\epsilon}_{in}$ (s^{-1})
20	displacement	0.360 mm/min	$1 \cdot 10^{-3}$
260	displacement	0.016 mm/min	$5 \cdot 10^{-5}$
330	displacement	0.016 mm/min	$5 \cdot 10^{-5}$
330	load	0.34 mm/min	$1 \cdot 10^{-3}$
330	load	34 mm/min	$8 \cdot 10^{-1}$
330	load	0.34 lbs/s	$8 \cdot 10^{-5}$
330	load	20 lbs/s	$1 \cdot 10^{-3}$
380	displacement	0.016 mm/min	$5 \cdot 10^{-5}$
380	load	0.34 lbs/s	$2 \cdot 10^{-4}$
380	load	20 lbs/s	$5 \cdot 10^{-3}$
380	load	200 lbs/s	$2 \cdot 10^{-2}$
380	load	2000 lbs/s	$2 \cdot 10^{-1}$

evidence of long-range crystallinity was found. While XRD measurements are not sensitive enough to detect a small volume fraction of nanometer-sized crystalline regions, transmission electron microscopy (TEM) also failed to reveal any evidence of crystallization. Differential scanning calorimetry (DSC) analysis of this material is provided elsewhere.^[5]

B. Tension Tests

1. Displacement-controlled tests

The engineering stress-strain curves for all samples tested under displacement control are plotted in Figure 1, along with their corresponding test conditions (i.e., temperature, displacement rate, and initial strain rate). It should be noted here that engineering stress-strain calculations were used, due to the lack of homogeneous flow found in samples that displayed macroscopic deformation, as will be discussed later.

True stress could not be rigorously calculated from load or displacement data without making the assumption that deformation is uniform. Samples denoted by arrows pointing toward the upper inset “gure failed in catastrophic shear, while samples denoted by arrows pointing toward the lower inset “gure failed in shear after extensive plastic macroscopic elongation, reduction of cross-sectional area, and necking. Samples that fractured in shear in these displacement-controlled tests did not display any measurable plastic macroscopic deformation prior to failure.

Also provided in Figure 1 are insets of the typical macro- and microscopic fractographs of samples tested at room temperature (20 C) and 330 C. The room-temperature test exhibited essentially no macroscopic ductility, but failed macroscopically in shear via a locally intense shear mechanism. Based on similar studies, it may be assumed that this strength and behavior is expected for all quasistatic loading conditions conducted on this or similar material at room temperature.^[5...7,43] The fracture surface (inset) shows the typical veined appearance of the locally ductile surface, consistent with other reports.^[4...7,34,37] The sample tested at 260 C failed in a similar manner, but with a slightly reduced fracture strength (i.e., $S_f = 1632$ MPa, $\sigma_y = 1792$ MPa, $\sigma_f = 1792$ MPa).

In contrast, samples tested at strain rates $5 \cdot 10^{-3} s^{-1}$ at 330 C and 380 C exhibited significantly reduced maximum strengths, as well as very high elongations to failure, almost failing via ductile rupture. Increasing the strain rate to $2 \cdot 10^{-1} s^{-1}$ at 330 C resulted in a return to macroscopic shear and a strength approaching that of samples tested at room temperature. It may be assumed that a significantly higher strain rate would

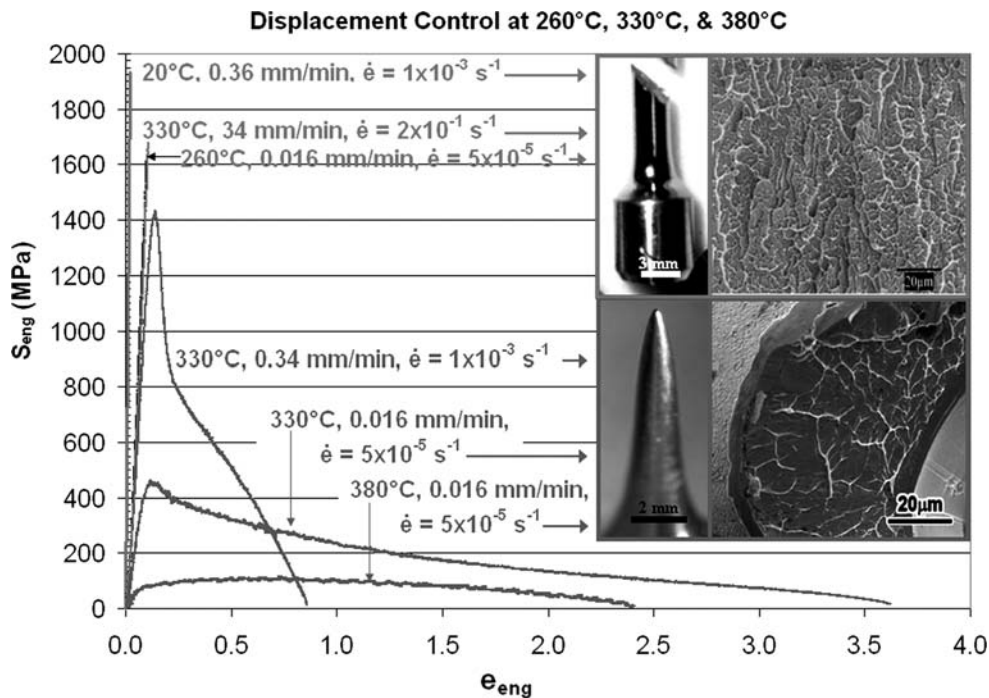


Fig. 1. Engineering stress-strain curves for all displacement-controlled tests. Insets show the typical macroscopic appearance of samples as well as a high-magnification view of the typical fracture surfaces.

be required to induce macroscopic shear at 380C conducted under displacement-controlled conditions, although this has not been tested as of the date of this publication.

2. Loading-rate-controlled tests

Figure 2 summarizes the engineering stress-strain curves for all samples tested under loading-rate-controlled conditions, with the sample tested under displacement control at room temperature provided for reference. Samples denoted by arrows pointing toward the upper inset "gure failed in catastrophic shear, with varying amounts of elongation ranging from negligible to significant. Samples denoted by arrows pointing toward the lower inset "gure failed after extensive necking and elongation, as shown in the inset.

At 330 C, samples failed in catastrophic shear at strain rates $8 \cdot 10^{-5} \text{ s}^{-1}$, with varying amounts of plastic macroscopic "ow observed prior to the catastrophic shear event. Catastrophic shear failure may have been avoided with more extensive macroscopic ductility at yet lower strain rates. At 380 C, samples displayed macroscopic "ow to failure via ductile rupture at strain rates $2 \cdot 10^{-2} \text{ s}^{-1}$, and catastrophic shear with negligible plastic macroscopic elongation at strain rates $2 \cdot 10^{-1} \text{ s}^{-1}$. The lower inset in Figure 2 also shows significant macro- and microscopic differences in the fracture of samples with high elongation tested in loading-rate control compared to the sample exhibited under displacement control.

C. Macroscopic Appearance

Figure 3 illustrates the four basic macroscopic appearances of the tension samples tested in displacement control and loading-rate control under different strain rates and test temperatures. The samples tested under displacement control at 20 C and 260 C failed in macroscopic shear with negligible macroscopic elongation, as seen in Figure 3(a). Samples tested at temperatures closer to the T_g (330 C, 380 C) in both displacement and loading-rate control at sufficiently high strain rates exhibited the same macroscopic appearance (i.e., Figure 3(a)).

Samples tested at relatively low strain rates at 330C and 380 C exhibited some degree of macroscopic plastic deformation, but the type depended on the loading condition. As seen in Figure 3(b), samples tested in displacement control at 330 C and 380 C gently necked nearly to a point, resembling completely ductile fracture in polycrystalline metals.^[36] Large pre-existing pores were observed on the fracture surfaces of the two samples tested at relatively lower strain rates, and may have prevented failure via ductile rupture, as seen by Wang et al.^[34] As seen in Figure 3(c), the samples tested in loading-rate control at 330 C displayed some necking and a reduction of area (RA), prior to catastrophic failure in shear. Samples tested in loading-rate control at 380C displayed rapid necking, but then transitioned to the relatively uniform elongation of a "ne ••wire•• of nearly constant diameter (e.g., 20 to 40 μm), as seen in Figure 3(d). The two samples tested at relatively low strain rates failed via ductile rupture, while a cavitated

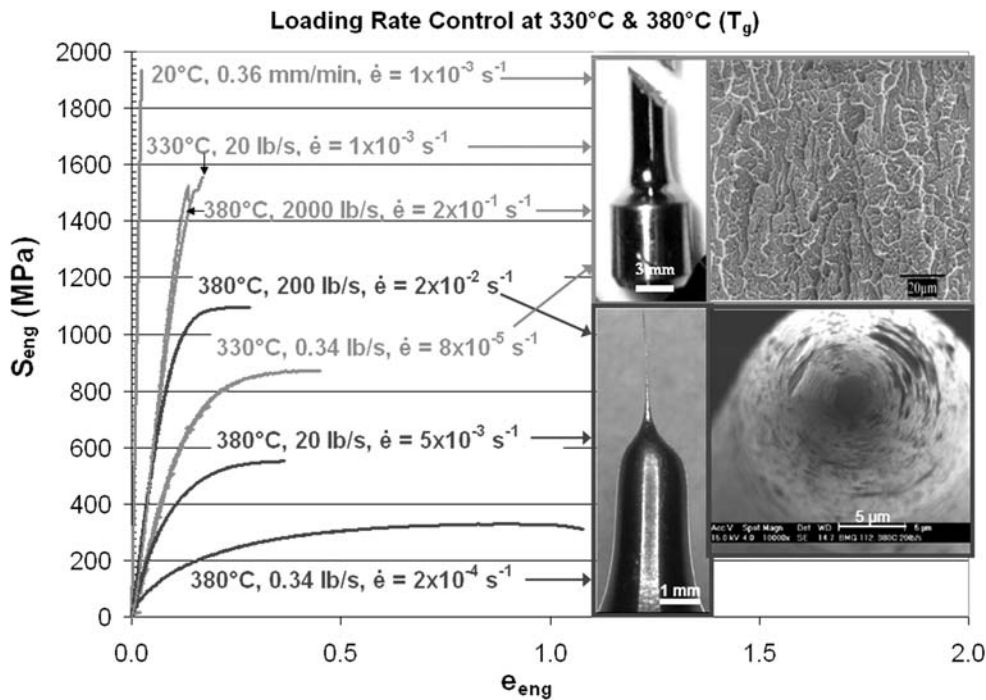


Fig. 2, Engineering stress-strain curves for all loading-rate-controlled tests, with the sample tested under displacement control at room temperature provided for reference. The dash-lined arrows extend the stress-strain curve to the measured values of the engineering fracture strain in the samples that exhibited the wirelike morphology. Insets show the typical macroscopic appearance of samples as well as a high-magnification view of the typical fracture surfaces.

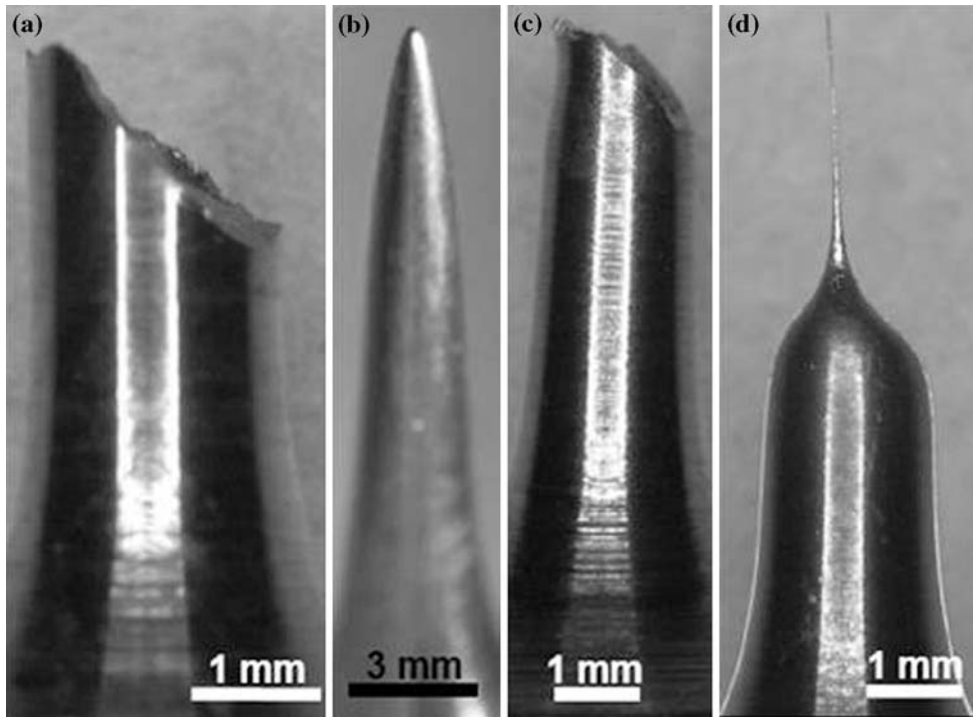


Fig. 3., Macroscopic morphologies of samples at the following temperatures and strain rates: a) displacement control: 20 C, $1 \cdot 10^{-3} \text{ s}^{-1}$; 260 C, $5 \cdot 10^{-5} \text{ s}^{-1}$; 330 C, $2 \cdot 10^{-1} \text{ s}^{-1}$; loading-rate control: 380 C, $2 \cdot 10^{-1} \text{ s}^{-1}$; (b) displacement control: 330 C, $5 \cdot 10^{-5} \text{ s}^{-1}$; 330 C, $1 \cdot 10^{-3} \text{ s}^{-1}$; 380 C, $5 \cdot 10^{-5} \text{ s}^{-1}$; (c) loading-rate control: 330 C, $8 \cdot 10^{-5} \text{ s}^{-1}$; 330 C, $1 \cdot 10^{-3} \text{ s}^{-1}$; and (d) loading-rate control: 380 C, $2 \cdot 10^{-4} \text{ s}^{-1}$; 380 C, $5 \cdot 10^{-3} \text{ s}^{-1}$; 380 C, $2 \cdot 10^{-2} \text{ s}^{-1}$.

fracture surface was observed on the sample tested at the highest loading rate. The length of this wire increased with increasing strain rate, until catastrophic shear was again produced at an effective initial strain rate of 10^1 s^{-1} .

IV. DISCUSSION

A. Hot Microhardness vs Tension Data

The strengths estimated from hot microhardness tests (via $\sigma_y = \text{VHN}/3 \text{ MPa}$ [45]) are plotted against the true yield stresses (σ_y) attained in tension tests at the same, or similar, test temperatures in Figure 4. Only data from tension tests conducted at a strain rate similar (i.e., within an order of magnitude) to that used in microhardness tests (i.e., $\sim 10^{-5} \text{ s}^{-1}$) were plotted. An exception is the stress value attained during testing in displacement control at room temperature, where the strain rate and loading condition are not expected to have an effect. The same general relationship between strength and temperature is observed in stresses attained from both microhardness and tension tests. However, the strengths achieved in tension tests were somewhat higher than those estimated from the microhardness data. The relative difference between the two strength values increased with increasing test temperature, deviating significantly beyond 260 C.

One reason for these differences in strength levels relates to the different loading condition being used in the different tests. Microhardness tests are conducted in

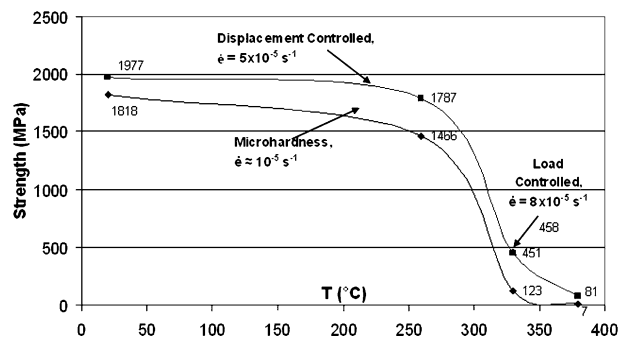


Fig. 4., Comparison of strengths estimated from hot microhardness (i.e., VHN/3) with the true yield stress attained in tension tests. Only data from tension tests conducted at a strain rate near that of the microhardness tests (i.e., $\sim 10^{-5} \text{ s}^{-1}$) at high temperatures are included. The solid lines were "fitted to the actual data points, to show the behavioral trend.

compression with the aid of a sharp indenter, inducing a combined compressive and hydrostatic stress state. A constant load (e.g., 300 g) is applied in a fixed amount of time, to allow penetration into the sample. However, the load is then held constant for a period of time (e.g., 15 seconds). This hold time typically has little effect on the indentation size and depth at low temperatures (relative to the T_g). However, at temperatures near the T_g , the material is able to flow considerably during the hold time, similar to a constant-load creep test. The size of the indentation may increase significantly during the hold time, producing a significantly lower microhardness and estimated strength. As an opposing

factor, hydrostatic compression has been shown to accelerate devitrification of BMGs, resulting in an increase in strength at higher test temperatures.^{46]}

In contrast, standard tension tests conducted in either displacement- or loading-rate-controlled conditions subject the sample to changing load conditions. The stress state is a combination of tensile and hydrostatic stresses, as opposed to the compressive and hydrostatic stress state induced by the hardness tests.^{47]} It should be clear that while hot microhardness testing provides a reasonable estimate of strength, the strength values estimated from microhardness tests are consistently lower at given test temperatures than those presently measured from tensile tests. In these cases, the difference in values cannot be normalized by the proportionality constant, since the microhardness tests and tensile tests each induce different deformation mechanisms, and they compete differently with increasing temperatures, as described earlier.

B. Strain-Rate Effects of Flow and Fracture Stress and Strain

1. Displacement control

Table II summarizes the tensile properties of samples tested in displacement control, under different temperature and strain-rate combinations. The displacement rate (dl/dt) was programmed in these displacement-controlled tests, whereas the effective load rate (dP/dt) and engineering stress rate (dS/dt) were calculated from the linear portion of the load-time curve. The engineering fracture strain was calculated from load-displacement data (ϵ_{MTS}) in all samples, and also from actual sample measurements (ϵ_{Meas}) in ductile samples. Values of ϵ_{Meas} were only slightly different than those of ϵ_{MTS} , indicating that nearly all load-displacement data to failure were collected and that machine compliance effects were small. The true plastic fracture strain (ϵ_f) and the RA were calculated from initial and final gage diameters. Samples with a measurable RA were

considered to exhibit some degree of macroscopic ductility (i.e., plastic deformation).

The engineering yield stresses (S_y) and engineering ultimate tensile strengths (S_{UTS}) were calculated from load data at the first measurable point of yielding and at the maximum load, respectively. The true yield stress (σ_y) and true stress at maximum load (σ_{UTS}) were calculated from the engineering stress values, assuming constancy of volume and uniform deformation. While constancy of volume assumptions cannot strictly be made when following Spaeper's free volume theory,^{8]} σ_y values were as accurate as possible given the current state of knowledge. Nonuniform deformation was not monitored, but could have occurred between the yield point and the maximum load. This, in addition to constancy-of-volume issues, makes S_{UTS} values less accurate than σ_y values.

A drop in engineering stress with increasing strain was observed in ductile samples tested at 330°C and 380°C at sufficiently low strain rates (i.e., Figure 1). Since it was not possible to image/measure the gage diameter during the original tests shown in Figure 1, it was unclear whether the stress drop past peak stress for the 330°C samples tested at 0.34 mm/min and 0.016 mm/min was due to the formation of a neck, the net generation of excess free volume, or some combination of the two. In order to address this, two separate interrupted tests were conducted under displacement-controlled conditions at 330°C at 0.34 mm/min on two separate pristine samples. The first sample was taken past the load/stress peak (σ_y , 1207 MPa) to an engineering stress of 992 MPa, and immediately unloaded and removed from the test chamber. This sample was effectively removed while in the steeply descending part of the stress-strain curve shown in Figure 1, in order to investigate the potential source(s) of the stress overshoot. The second sample was taken past the second knee in the curve, at an engineering stress of 702 MPa, and immediately unloaded and removed from the test chamber. This second sample was effectively removed in the less steeply descending part of the stress-strain curve in Figure 1.

Table II. Tensile Properties of Samples Tested in Displacement Control

T	20	260	330	330	330	380	C
dl/dt	0.36	0.016	0.016	0.34	34	0.016	mm/min
dP/dt	132	0.58	0.34	11.1	3430	0.012	lb/s
$\dot{\epsilon}_{\text{in}}$	$1 \cdot 10^{-3}$	$5 \cdot 10^{-5}$	$5 \cdot 10^{-5}$	$1 \cdot 10^{-3}$	$2 \cdot 10^{-1}$	$5 \cdot 10^{-5}$	s^{-1}
$\dot{\epsilon}_t$	$1 \cdot 10^{-3}$	$4 \cdot 10^{-5}$	$1 \cdot 10^{-5}$	$7 \cdot 10^{-4}$	$1 \cdot 10^{-1}$	$1 \cdot 10^{-5}$	s^{-1}
dS/dt	19	0.17	0.04	3.67	1185	0.003	MPa/s
S_y	1933	1632	415	1250	1680	75	MPa
S_{UTS}	1933	1632	497	1435	1681	122	MPa
σ_y	1977	1787	451	1380	1855	81	MPa
σ_{UTS}	1978	1792	558	1635	1860	242	MPa
ϵ_y	2 pct	10 pct	9 pct	11 pct	11 pct	8 pct	"
ϵ_{MTS}	2 pct	10 pct	362 pct	86 pct	13 pct	241 pct	"
ϵ_{Meas}	NA*	NA	359 pct	91 pct	NA	251 pct	"
ϵ_f	0 pct	0 pct	544 pct	455 pct	12 pct	768 pct	"
RA	0 pct	0 pct	99.6 pct	98.9 pct	0 pct	99.95 pct	"
failure mode	catastrophic shear	catastrophic shear	ductile, shear	ductile, shear	catastrophic shear	ductile, shear	"

*Not applicable.

Low- and intermediate-magnification SEM examination was used to measure the dimensions of each sample, in addition to examining for the presence of any neck. The first sample did not exhibit any evidence of localized flow or perceptible neck, although a small neck was visible in the second sample examined at magnifications up to 40X in the SEM. The lack of neck in the first sample indicates that globally homogeneous flow occurred in the first sample, and strongly supports the contentions^[4,23,25] that such stress overshoots correspond to the generation of excess free volume. The second sample, unloaded just past the second knee in the stress-strain curve, clearly indicates the presence of a small neck and the beginnings of globally inhomogeneous flow. The change (i.e., decrease in steepness) in the slope of the stress-strain curve compared to the steeply descending slope immediately after the peak stress could result from the localization of flow (i.e., necking) producing a higher local strain rate (due to the reduction in effective gage length) in this regime, eventually producing the macroscopic appearance shown in the inset to Figure 1. Measurement of the sample diameters in these interrupted samples revealed the engineering stresses in the first and second samples to be 992 and 702 MPa and true stresses in the first and second samples to be 1070...1116 and 900...1005 MPa, respectively.

The engineering strain rate near the fracture event ($\dot{\epsilon}_f$) was estimated from the displacement data obtained just before failure. These values were somewhat lower than the initial strain rates ($\dot{\epsilon}_{in}$), as the gage length was continuously increasing while the displacement rate remained constant per unit time. Figure 5 plots the effective (evolving) strain rate as a function of engineering strain for a single displacement- and load-controlled test. The evolution of the strain rate had a direct effect on the failure behavior and stability of deformation. Deformation of ductile samples occurred under a constant displacement rate and a slowly decreasing strain rate, as the load was allowed to decrease in response to the loss of cross-sectional area (\dot{A}). The rate of loss of area with respect to the increase in longitudi-

dinal strain ($dA/d\epsilon$) increased slightly until the failure event was approached, where the area was reduced more rapidly. This produced the macroscopic appearance of the slightly convexly tapered samples observed in Figure 3(b).

2. Loading-rate control

Table III summarizes the tensile properties of samples tested in loading-rate control under different temperature and strain-rate combinations. The load rate (dP/dt) was programmed in these loading-rate-controlled tests, whereas the displacement rate (d/dt), engineering stress rate (dS/dt), and effective initial strain rate ($\dot{\epsilon}_{in}$) were calculated from the linear portions of the load-time curves. The ϵ_{MTS} and ϵ_{Meas} were calculated as described earlier. Values of ϵ_{Meas} in ductile samples were significantly higher than those of ϵ_{MTS} , because the elongation due to wire formation could not be recorded from the displacement of the MTS actuator. The true plastic strain at fracture (ϵ_f), RA, S_y , S_{UTS} , σ_y , and σ_{UTS} were calculated in the manner described earlier, with the same issues affecting the accuracy of the true stress calculations. At a given test temperature, the RA and ϵ_{MTS} decreased with increasing strain rate. Stress overshoots were not observed, due to the nature of a loading-rate-controlled test, in which a constantly increasing load is applied and load relaxation is not allowed.

At a given test temperature and approximately the same initial strain rate, S_y and σ_y values attained in load-controlled tests were similar to those attained in displacement-controlled tests. This is expected, since the effective strain rate of tests conducted in loading-rate control remains similar to the initial effective strain rate of the displacement-controlled tests, up to the yield point of the material. However, once significant cross-sectional area is lost, the actuator further increases the displacement strain rate to keep the loading-rate constant. This resulted in much higher S_{UTS} and σ_{UTS} values in samples tested in loading-rate control compared to those tested in displacement control, at the same temperature and similar initial strain rates.

As shown in Figure 5, the strain rate near fracture ($\dot{\epsilon}_f$) is much higher than the initial strain rate in load-controlled tests. The MTS actuator accelerates its displacement rate to maintain a constant load increase per unit time, while the sample cross section continuously decreases. In loading-rate-controlled tests in which significant macroscopic flow occurred, the final strain rates were two to three orders of magnitude higher than the initial strain rates calculated from linear displacement data (i.e., $\dot{\epsilon}_{in}$). In the case of the sample tested at 330 C and 0.34 lb/s, the strain rate was initially low enough to allow inhomogeneous viscous flow (i.e., necking), but transitioned to localized inhomogeneous flow via catastrophic shear at a final strain rate estimated to be approximately $3 \cdot 10^3 \text{ s}^{-1}$. This non-uniform flow prior to maximum load makes the calculated σ_{UTS} values particularly inaccurate, but illustrates that necking can precede catastrophic shear fracture under certain test conditions. In this case, a 32 pct RA preceded catastrophic shear failure.

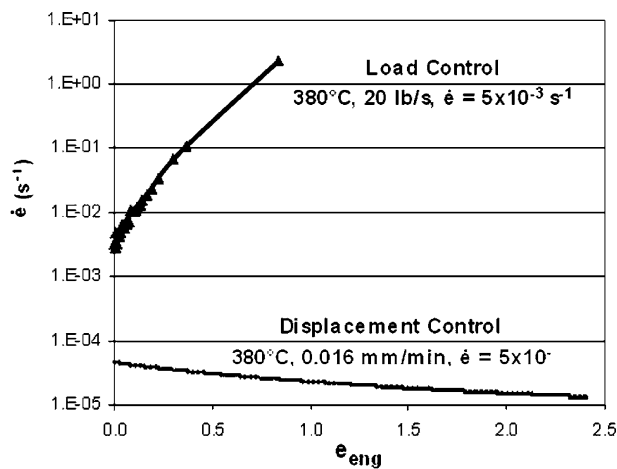


Fig. 5. Engineering strain rate plotted as a function of engineering strain, based on intervals of displacement data and evolving gage lengths of the sample.

Table III. Tensile Properties of Samples Tested in Load Control

T	20	330	330	380	380	380	380	C
dI/dt	0.36	0.022	0.337	0.077	6.2	20.9	51.4	mm/min
dP/dt	132	0.34	20	0.34	20	200	2000	lb/sec
$\dot{\epsilon}_{in}$	$1 \cdot 10^{-3}$	$8 \cdot 10^{-5}$	$1 \cdot 10^{-3}$	$2 \cdot 10^{-4}$	$5 \cdot 10^{-3}$	$2 \cdot 10^{-2}$	$2 \cdot 10^{-1}$	s^{-1}
$\dot{\epsilon}_f$	$1 \cdot 10^{-3}$	$3 \cdot 10^{-3}$	$4 \cdot 10^{-3}$	$1 \cdot 10^{-2}$	$2 \cdot 10^{00}$	$4 \cdot 10^{00}$	$8 \cdot 10^{-1}$	s^{-1}
dS/dt	19	0.10	2.50	0.11	5.67	57.74	577.43	MPa/s
S_y	1933	425	1050	80	245	500	1000	MPa
S_{UTS}	1933	871	1555	329	554	1142	1527	MPa
σ_y	1977	458	1140	82	257	520	1077	MPa
σ_{UTS}	1978	1195	1798	541	891	2124	1721	MPa
ϵ_y	2 pct	8 pct	9 pct	3 pct	5 pct	4 pct	8 pct	"
ϵ_{MTS}	2 pct	45 pct	17 pct	108 pct	36 pct	25 pct	14 pct	"
ϵ_{Meas}	NA*	NA	NA	151 pct	114 pct	128 pct	NA	"
ϵ_f	0 pct	36 pct	3 pct	1523 pct	1312 pct	1229 pct	0 pct	"
RA	0 pct	30.2 pct	3.1 pct	99.99998 pct	99.9998 pct	99.9995 pct	0 pct	"
l_{wire}	NA	NA	NA	1.7	2.5	5.2	NA	mm
failure mode	catastrophic shear	ductile, shear	ductile, shear	drawing, ductile rupture	drawing, ductile rupture	drawing, near-ductile rupture	catastrophic shear	"

*Not applicable.

A different flow-fracture morphology transition occurred in samples tested at 380C at the same initial strain rates that greatly limited macroscopic deformation at 330 C. While these samples were necking, they experienced a rapidly increasing (i.e., ~100 times) displacement rate and strain rate, due to the nature of loading-rate-controlled testing. During this rapid increase in strain rate, no load drop was permitted, despite a rapidly decreasing cross-sectional area. The loss of cross-sectional area with respect to the increase in longitudinal strain ($dA/d\epsilon$) was initially very high, but decreased rapidly. As further elongation occurred and strain rate increased rapidly, a nearly-constant-diameter wire was produced (e.g., 20 to 40 μ m), where $dA/d\epsilon$ remained slightly negative and nearly constant until failure occurred. This produced the flow-fracture morphology seen in Figure 3(d).

C. General Flow Behavior

1. Newtonian vs non-Newtonian flow

Samples tested in either displacement control or loading-rate control exhibited inhomogeneous macroscopic deformation in certain T- $\dot{\epsilon}$ regimes, as evidenced by the necklike formations seen in Figure 3. Because a steady-state stress was not observed, yield stresses were used to determine Newtonian flow behavior. Compared to the ultimate stress, yield stress is not greatly affected by loading condition (load vs displacement control) at a given temperature and initial strain rate, for the reasons mentioned earlier. A schematic plot of σ_y vs $\dot{\epsilon}$ for all samples is shown in Figure 6(a). At a given test temperature, σ_y increased linearly with strain rate, until a sufficiently high strain rate was used to cause failure via catastrophic shear without measurable plastic macroscopic deformation. At this point, the maximum strength attained at room temperature is approached and linearity is lost.

The linear increase of σ_y with $\dot{\epsilon}$ (i.e., $\tau / \dot{\gamma}^{[27]}$) at lower strain rates suggests that Newtonian flow occurred over the range of T and $\dot{\epsilon}$ presently tested. However, the strain-rate-sensitivity value was calculated ($\nu_{am} = (\Delta \log \sigma) / (\Delta \log \dot{\epsilon})$) to be 0.34 and 0.35, at 330C and 380 C, respectively. Thus $\nu_{am} < 1$, and flow was non-Newtonian. It should be noted that, when using only engineering peak stress values, a similar ν_{am} value of 0.31 was calculated for displacement-controlled tests conducted at 330 C. Viscosity (η) was calculated as one-third the ratio of the σ_y divided by the initial strain rate (i.e., $\eta = \sigma_y / (3\dot{\epsilon})$)^[48,49] and is plotted vs strain rate in Figure 6(b). Viscosity is seen to decrease with increasing strain rate, whereas the viscosity of a Newtonian fluid is independent of strain rate, again showing that flow was non-Newtonian.

It may be considered that the localized deformation observed in samples tested in loading-rate-controlled conditions could have been induced by a locally higher temperature at the center of the gage length (i.e., due to a general loss of strength with increasing temperature). As noted in the experimental section of this article, the oven used is uniform to ± 3 K, and loading was not initiated until the temperature at the back of the oven chamber and adjacent to the sample were equal. However, no thermocouples were in direct contact with the samples at the center and outer regions of the gage lengths to record what temperature variation actually existed here. Thus, small temperature variations on the order of a few degrees, or those induced by deformation heating,^[50] could contribute to this observation. Such effects could produce the subtle temperature differences between the grips/heads and the center of the tensile specimen tested at similar effective engineering strain rates, in both displacement- and loading-rate-controlled tests throughout this study.

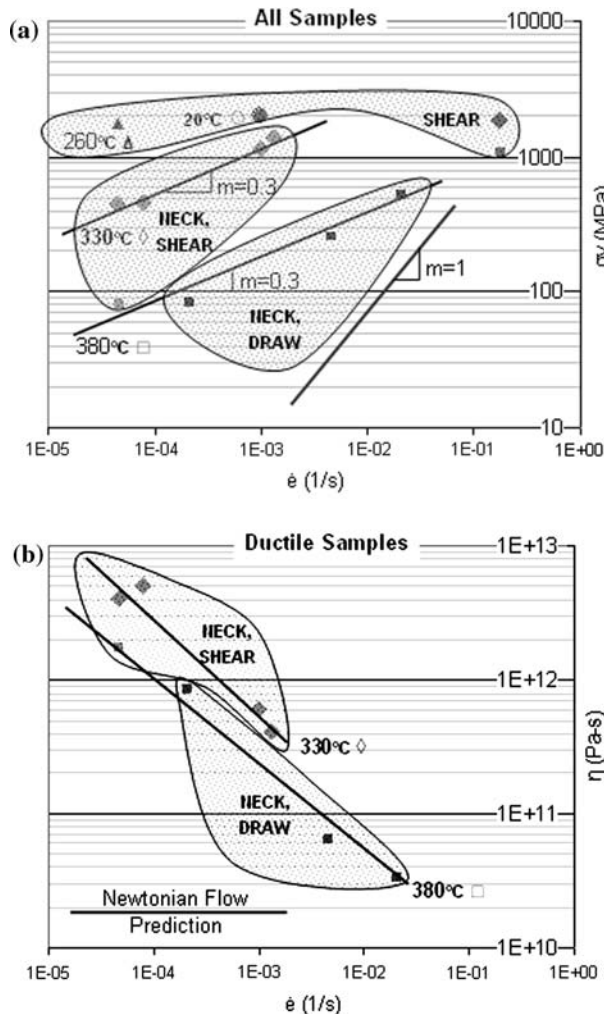


Fig. 6. The effect of initial strain rate on yield stress in (a) all samples and (b) just samples where macroscopic deformation was observed. The predicted Newtonian flow is provided (b) as a solid horizontal. Macroscopic appearance (shear, neck + shear, neck + draw) is also provided.

2. Macroscopic deformation-mechanism maps constructed from present data

The different evolution of strain rate in the tension tests conducted in displacement control vs loading-rate control produces significantly different flow behavior and sample appearances. This is shown by the separate schematic macroscopic deformation-mechanism maps for each loading condition provided in Figures 7(a) and (b), following the format used by other authors.^[4,23,24] Figure 7(a) shows the two inhomogeneous flow regimes exhibited by samples tested in displacement control: (1) shear localization (inhomogeneous flow with no macroscopic deformation) and (2) macroscopic inhomogeneous flow (inhomogeneous flow with macroscopic deformation). Data from displacement-controlled tension tests conducted by Lee et al.^[24] are also included and are consistent with the macroscopic flow regimes depicted. Homogeneous flow may be encouraged at even higher temperatures or lower strain rates than those tested, although crystallization could become an issue in these conditions.

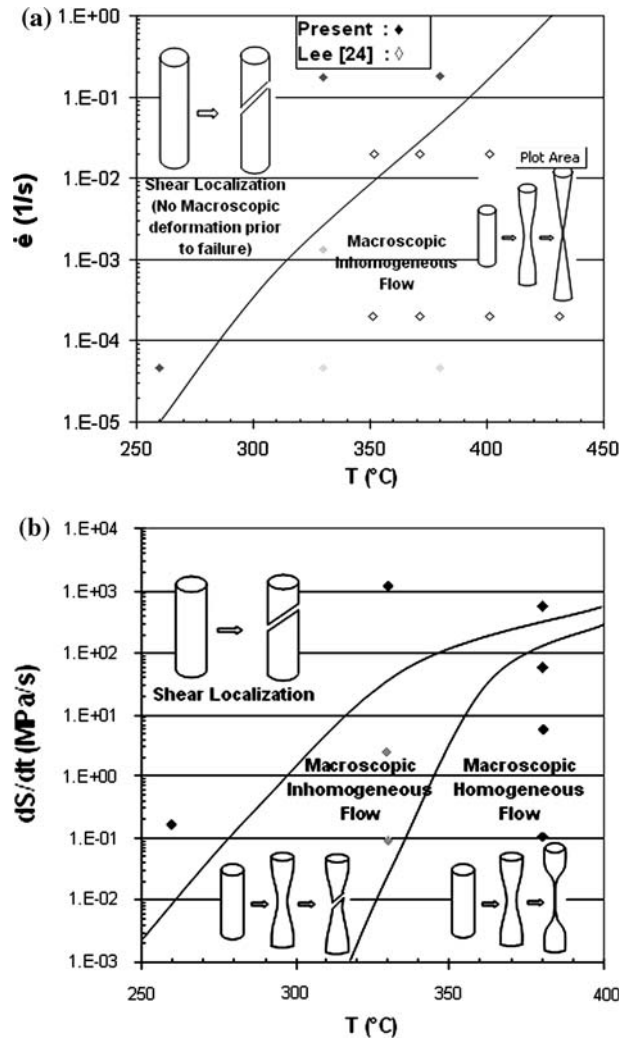


Fig. 7. A proposed deformation-mechanism map for tension tests presently conducted in (a) displacement control and (b) loading-rate control. Flow transitioned from inhomogeneous to homogeneous in the region to the furthest right in (b).

Three distinct regimes were found in samples tested in loading-rate control, as illustrated in Figure 7(b): (1) shear localization, (2) macroscopic inhomogeneous flow, and (3) uniform flow (homogeneous deformation after an initial neck resulting in the wire morphology). Because the strain rate changes significantly from the beginning to the end of a load-controlled tension test, the engineering stress rate (dS/dt) was plotted vs test temperature in this deformation-mechanism map. This information is also listed in Table IV.

Schematic macroscopic deformation-mechanism maps of LM1 have also been constructed by Lu et al.^[4] in compression and Wang et al.^[34] in tension. The regions proposed by Lu et al.^[4] were as follows: (1) shear localization (inhomogeneous), (2) non-Newtonian flow (homogeneous), and (3) Newtonian (homogeneous) flow. The three regions reported by Wang et al.^[34] were as follows: (1) inhomogeneous (i.e., shear with no prior macroscopic deformation), (2) transition region (i.e., inhomogeneous necking followed by shear), and (3)

Table IV. Fracture Morphology at Different Loading Rates and Conditions

Control Type	T (C)	Neck and Shear	Neck, Draw, and Ductile Rupture	Neck, Draw, and Near-Ductile Rupture	Catastrophic Shear
Displacement	330	$5 \cdot 10^{-5} \leq \dot{\epsilon} \leq 1 \cdot 10^{-3} \text{ s}^{-1}$			$\dot{\epsilon} > 2 \cdot 10^{-1} \text{ s}^{-1}$
Displacement	380	$\dot{\epsilon} = 5 \cdot 10^{-5} \text{ s}^{-1}$			
Load	330	$0.34 \leq P \leq 20 \text{ lb/s}$			
Load	380		$0.34 \leq P \leq 20 \text{ lb/s}$	$P = 200 \text{ lb/s}$	$P > 2000 \text{ lb/s}$

homogeneous (i.e., superplastic, uniform deformation necking to a point). Displacement-controlled tension data from the present study as well as those of Lee et al.^[24] are superimposed over the deformation-mechanism maps of Lu and Wang in Figures 8(a) and (b), respectively. Samples that failed in catastrophic shear without plastic macroscopic deformation fall into the region at the furthest left, in general agreement with the regimes depicted in both macroscopic deformation-mechanism maps (i.e., References 32 and 34). Samples that failed after measurable plastic deformation gener-

ally occurred to the right of the region at the furthest left. However, non-Newtonian inhomogeneous flow was found to occur in both the middle regime and the regime at the furthest right of the proposed deformation-mechanism maps, disagreeing with both References 32 and 34. In summary, the maps from Lu et al.^[4] and Wang et al.^[34] could not be used to predict the type of plastic macroscopic tensile flow that occurred in the present study or in the study by Lee et al.^[24] In addition, tensile flow was found to be non-Newtonian in the Newtonian flow regions obtained during compression studies by Lu et al.^[4]

3. Superplastic behavior

While elongations of well over 100 pct occurred in displacement-controlled tension tests conducted at 330 C and 380 C, these samples deformed nonuniformly to failure. Therefore, no true superplastic behavior was exhibited in displacement-controlled tension tests. Samples tested at sufficiently low strain rates in loading-rate control at 380 C also necked, but not to failure. Despite initial nonuniform flow (i.e., necking), these samples met the definition of superplastic behavior by maintaining their incipient necks and deforming uniformly beyond that point. These samples elongated 114 to 151 pct, then failed via ductile rupture or cavitation after a very large RA. It may also be noted that the superplastic behavior was encouraged at intermediate strain rates, where the longest length wire was produced at an initial effective strain rate of $2 \cdot 10^{-2} \text{ s}^{-1}$, while a shorter wire was produced at $5 \cdot 10^{-3} \text{ s}^{-1}$, and no wire at all at $2 \cdot 10^{-1} \text{ s}^{-1}$.

V. CONCLUSIONS

The authors observed and analyzed the effects of test temperature, loading rate, and loading condition on the global deformation behavior of the LM1 BMG in tension. In general, lower strain rates and higher test temperatures encouraged more extensive and sustained flow in addition to the following conclusions.

1. Samples fractured in shear without macroscopic deformation at all loading conditions tested from room temperature to 260 C. Samples tested at 330 C and 380 C at sufficiently low strain rates in either displacement or loading-rate control exhibited measurable macroscopic deformation, and fractured in shear or ductile rupture. Samples tested at 330 C and 380 C with sufficiently high strain rates

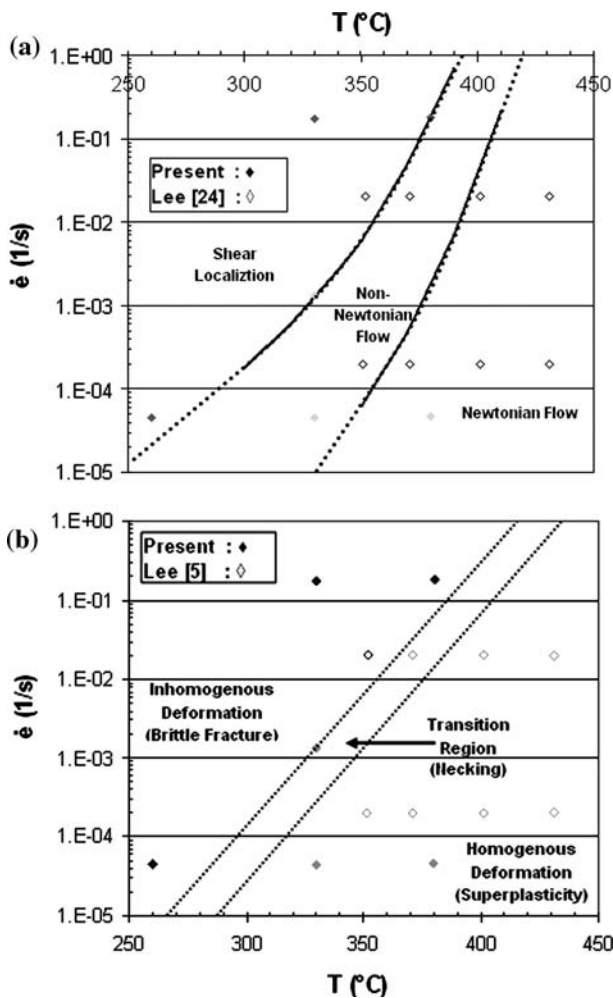


Fig. 8. Deformation-mechanism maps of (a) Lu et al.^[4] and (b) Wang et al.^[34] with data from the present study and from Lee et al.^[24] superimposed.

in either displacement or loading-rate control again failed in shear without macroscopic deformation.

2. Macroscopic flow occurred in significantly different fashions in displacement control and loading-rate control.
 - a. Samples tested in displacement control exhibited inhomogeneous and non-Newtonian flow at 330 C and 380 C, a result of a gentle necking to failure. A maximum elongation of 360 pct was achieved at a test temperature of 330 C and a strain rate of $5 \cdot 10^{-5} \text{ s}^{-1}$. The interrupted tests clearly revealed that the initial stress drop after peak stress was not due to the formation of a neck, supporting the idea of the stress-induced generation of free volume. Continued deformation of a sample well past the peak stress eventually revealed the presence of a neck, followed by subsequent localization of flow in that region.
 - b. Samples tested in loading-rate control exhibited inhomogeneous and non-Newtonian flow (i.e., necked and failed in shear) at 330C, in all the loading rates tested. Samples tested at 380 C initially flowed inhomogeneously (i.e., necked), but then transitioned to homogeneous flow (i.e., uniform) as the strain rate increased, resulting in a drawn out wire of nearly constant (i.e., 20- to 40 μm) diameter. A maximum length wire of 5 mm was achieved at a test temperature of 380C and an initial strain rate of $2 \cdot 10^{-2} \text{ s}^{-1}$, a final strain rate of $2 \cdot 10^0 \text{ s}^{-1}$, and a stress rate of 58 MPa/s. An engineering stress drop could not be observed, due to the nature of a load-controlled test. Slight local temperature variations may contribute to this observation.
3. The present results have implications for deformation processing in the supercooled liquid regime. Due to the large differences in strain-rate evolution, deformation-processing conditions in loading-rate control would have to be significantly different than those utilized in displacement control to achieve similar material behavior. No large-scale homogeneous deformation was observed at the loading conditions, strain rates, and temperatures tested. This is undesirable from a deformation-processing standpoint, as geometric instabilities create thin spots during bending operations. However, homogeneous flow was observed on a smaller scale in the formation of nearly-constant-diameter wires. This was observed in tests conducted in loading-rate control at 380 C, at an engineering stress rate between 0.11 and 58 MPa/s, with the length of the stable wire increasing with the increased stress rate.

ACKNOWLEDGMENTS

The authors express great appreciation to Liquid-metal Technologies and the Army Research Labs for the supply of materials, as well as to the Army

Research Laboratory Grant No. ARO-DAAD19-02-1-0364, the Office of Naval Research Grant No. ONR-N00014-03-1-0205, and the CWRU BS/MS Fellowship. The authors also thank Dr. Yi Liu and Dr. Dingqiang Li for their stunning electron microscopy images, and Ali Shamimi Nouri for his understanding and study of the thermal-mechanical properties of these metallic glasses. The authors cannot underestimate the technical support of Chris Tuma in providing mechanical testing system instructions and solutions.

REFERENCES

1. W.H. Wang, C. Dong, and C.H. Sheck: *Mater. Sci. Eng., R*, 2004, vol. 44, pp. 44...89.
2. A. Peker and W.L. Johnson: *Appl. Phys. Lett.*, 1993, vol. 63, pp. 2342...44.
3. A. Mashur, R. Busch, and W.L. Johnson: *J. Non-Cryst. Solids* 1999, vol. 252, Part 2, pp. 566...71.
4. J. Lu, G. Ravichandran, and W.L. Johnson: *Acta Mater.*, 2003, vol. 51, pp. 3429...43.
5. P. Lowhaphandu, L.A. Ludrosky, and J.J. Lewandowski: *Intermetallics* 2000, vol. 8, pp. 487...92.
6. P. Lowhaphandu, S.L. Montgomery, and J.J. Lewandowski: *Scripta Mater.*, 1999, vol. 41, pp. 19...24.
7. J. Wadsworth and T.G. Nieh: in *Superplasticity, Current Status and Future Potential* P.B. Berbon, T. Sakuma and T.G. Langdon, eds., MRS, Boston, MA, 1999, vol. 601, pp. 141...51.
8. F. Spaepen: *Acta Mater.*, 1979, vol. 25, pp. 407...15.
9. H. Eyring: *J. Chem. Phys.*, 1936, vol. 4, pp. 283...91.
10. A.S. Argon: *Acta Metall.*, 1979, vol. 37, pp. 47...58.
11. H.A. Bruck, T. Christman, A.J. Rosakis, and W.L. Johnson: *Scripta Mater.*, 1994, vol. 30, pp. 429...34.
12. J.J. Lewandowski and P. Lowhaphandu: *Philos. Mag. A*, 2002, vol. 82, pp. 3427...41.
13. G. Sunny, J.J. Lewandowski, and V. Prakash: *J. Mater. Res.*, 2007, vol. 22, pp. 389...401.
14. H.S. Chen: *Acta Metall.*, 1974, vol. 22, pp. 1505...11.
15. H.S. Chen and C.E. Miller: *Rev. Sci. Instrum.*, 1970, vol. 41, pp. 1237...38.
16. J.J. Lewandowski, W.H. Wang, and A.L. Greer: *Philos. Mag. Lett.*, 2005, vol. 85, pp. 77...87.
17. Y.H. Liu, G. Wang, R.J. Wang, D.Q. Zhao, M.X. Pan, and W.H. Wang: *Science* 2007, vol. 315, pp. 1385...88.
18. J. Schroers and W.L. Johnson: *Phys. Rev. Lett.*, 2004, vol. 93, p. 255506.
19. V. Ponnambalam, J.S. Poon, and G.J. Shi: *J. Mater. Res.*, 2004, vol. 19, pp. 1320...23.
20. W.H. Wang: *J. Appl. Phys.*, 2006, vol. 99, p. 093506.
21. M. Li, J. Eckert, L. Kecskes, and J.J. Lewandowski: *J. Mater. Res.*, 2007, vol. 22, pp. 255...57.
22. C.L. Chiang, J.P. Chu, C.T. Lo, T.G. Nieh, Z.X. Wang, and W.H. Wang: *Intermetallics* 2004, vol. 12, pp. 1057...61.
23. K.S. Lee and Y.W. Chang: *Met. Mater. Int.*, 2005, vol. 11, pp. 53...57.
24. K.S. Lee and Y.W. Chang: *Mater. Sci. Eng., A*, 2005, vol. 399, pp. 238...43.
25. M. Bletry, P. Guyot, Y. Brechet, J.J. Blandin, and J.L. Soubeyrou: *Mater. Sci. Eng., A*, 2004, vol. 389, pp. 1005...11.
26. M. Bletry, P. Guyot, Y. Brechet, J.J. Blandin, and J.L. Soubeyrou: *Intermetallics* 2004, vol. 12, pp. 1051...55.
27. Y.A. Cengal and R.H. Turner: *Thermal-Fluid Sciences* McGraw-Hill, New York, NY, 2005, p. 471.
28. Y. Kawamura, T. Shibita, A. Inoue, and T. Masumoto: *Scripta Mater.*, 1997, vol. 37, pp. 431...36.
29. P.D. Hey, J. Sietsma, and A.V.D. Beukel: *Acta Mater.*, 1998, vol. 46, pp. 5873...82.
30. Y. Kawamura, T. Nakamura, and A. Inoue: *Scripta Mater.*, 1998, vol. 39, pp. 301...06.
31. A.R. Leonhard, M. Heilmaier, and J. Eckert: *Scripta Mater.*, 2000, vol. 43, pp. 459...64.

32. K.S. Lee, T.K. Ha, S. Ahn, and Y.W. Chang: *J. Non-Cryst. Solids* 2003, vol. 317, pp. 193...99.
33. T.G. Nieh, J. Wadsworth, C.T. Liu, T. Ohkubo, and Y. Hirotsu: *Acta Mater.*, 2001, vol. 49, pp. 2887...96.
34. G. Wang, J. Shen, J.F. Sun, Z.P. Lu, Z.H. Stachurski, and B.D. Zhou: *Intermetallics* 2005, vol. 13, pp. 642...48.
35. Y. Kawamura, T. Shibata, A. Inoue, and T. Masumoto: *Mater. Trans., JIM*, 1999, vol. 40, pp. 335...42.
36. G.E. Dieter: *Mechanical Metallurgy*, McGraw-Hill, New York, NY, 1986, p. 242.
37. T.G. Nieh, T. Mukai, C.T. Liu, and J. Wadsworth: *Scripta Mater.*, 1999, vol. 40, pp. 1021...27.
38. W.A. Backofen: in *Deformation Processing* M. Cohen, ed., Addison-Wesley Publishing Co., Inc., Taclaban City, Philippines, 1972, pp. 207...10.
39. R. Hertzberg: *High-Temperature Deformation Response of Crystalline Solids. Deformation and Fracture Mechanics of Engineering Materials*, Wiley, New York, NY, 1995, pp. 175...78.
40. P. Lowhaphandu: Ph.D. Thesis, Case Western Reserve University, Cleveland, OH, 2000.
41. R. Busch, Y.J. Kim, and W.L. Johnson: *J. Appl. Phys.*, 1995, vol. 77, pp. 4039...43.
42. J.J. Lewandowski, M. Shazly, and A.S. Nouri: *Scripta Mater.*, 2006, vol. 54, pp. 337...41.
43. T.G. Nieh, C. Schuh, J. Wadsworth, and Y. Li: *Intermetallics* 2002, vol. 10, pp. 1177...82.
44. ASTM E8-04, *Standard Test Methods for Tension Testing of Metallic Materials*, ASTM, Philadelphia, PA, 2004, vol. E8-04.
45. G.E. Dieter: *The Hardness Test: Mechanical Metallurgy* McGraw-Hill, New York, NY, 1986, p. 330.
46. B.C. Ko, P. Wesseling, L.O. Vatamanu, G.S. Shi"et, and J.J. Lewandowski: *Intermetallics* 2002, vol. 10, pp. 1099...1103.
47. J.J. Lewandowski and P. Lowhaphandu: *Int. Mater. Rev.*, 1998, vol. 43 (4), pp. 145...87.
48. G.W. Scherer: *Relaxation in Glass and Composites* Krieger Publishing, Maber, FL, 1992.
49. R.K. Gupta: *Polymer and Composite Rheology* Marcel Dekker, New York, NY, 2000.
50. J.J. Lewandowski and A.L. Greer: *Nat. Mater.*, 2006, vol. 5, pp. 15...18.